SPATIALLY AND TEMPORALLY RESOLVED HARMONIC EMISSION STUDIES OF LASER PLASMAS

Report No. 68

Steven M. Jackel

ACKNOWLEDGEMENT

The research reported on herein was supported by the following principal sponsors:

Exxon Research & Engineering Company
General Electric Company
Northeast Utilities Company
University of Rochester

Other contributors to the efforts of the work in the Laboratory for Laser Energetics include:

Empire State Electric Energy Research Company
U.S. National Science Foundation
New York State Energy Research & Development Administration
New York State Science & Technology Foundation
U.S. Air Force Office of Scientific Research

Such support does not imply endorsement of the content by any of the above parties.

DECEMBER 1977

ABSTRACT

Harmonic light emission from laser produced plasmas at the second and three-halves harmonics of the incident laser light frequency were spatially and temporally resolved to directly provide critical and quarter-critical electron density trajectories ($n_{e\ cr}=10^{21}\ cm^{-3}$ and $n_{e\ \frac{1}{4}cr}=2.5\times10^{20}\ cm^{-3}$ for $\lambda_{LASER}=1.06\mu m$). The harmonic emissions were viewed from a direction perpendicular to the irradiation plane of a four beam laser.

The neodymium:glass laser, used to irradiate spherical-shell laser-fusion targets, provided focused $1.06\mu m$ wavelength light of intensity $I_{LASER} \lesssim 10^{15}\ \frac{watt}{cm^2}$ in pulses of durations τ_{FWHM}=100-600 psec and rise time τ_{RISE}(10%-max)=40-230 psec.

The experimental data was applied to the study of laser light absorption and plasma energy transport. Absorption was found to vary by a factor of two for a factor of four increase in the measured distance between the critical and quarter-critical densities. Calculation of collisional plus resonant absorption gave a good fit. Moderate profile modification ($n_{jump}/n_{cr} \gtrsim .7$) was predicted to not substantially alter the scalelength dependence of absorption. The rate and nature of plasma energy transport was shown to affect the ablation region density profile, including the critical and quarter-critical density locations. Theory and experiment agreed in the prediction of a unique peak excursion relationship. Results suggested a laser pulse rise time dependence to the energy trans-

port contributing to ablation with longer rise time pulses giving larger values for the transport.

To obtain results with an accuracy necessary for the study of laser-plasma interaction physics, it was found that accuracy enhancement beyond the resolution of the optical system was needed. A simple image technique was devised to significantly enhance the accuracy of edge location measurements. Application of the image analysis technique required the determination of the optical system spatial resolution. The streak camera spatial resolution was studied and its point spread response was measured as a function of input intensity.

Publications

The following publications related to this study have appeared during the course of this report work.

Steven Jackel, James Albritton, and Edward Goldman "Critical-Density Scalelength Measurements in Laser Produced Plasmas" Phys. Rev. Letters 35, 514 (1975)

Steven Jackel, Bruce Perry, and Moshe Lubin "Dynamics of Laser Produced Plasmas through Time-Resolved Observations of the $2\omega_o$ and $(3/2)\omega_o$ Harmonic Light Emissions" Phys. Rev. Letters 37, 95 (1976)

W. Friedman, S. Jackel, W. Seka and J. Zimmermann "Dynamic Range and Spatial Measurements of Psec. Streak Cameras" in Proceedings of the 12th International Congress on High Speed Photography, (1977)

TABLE OF CONTENTS

LIST OF TABLES

LIST OF FIGURES

Page

Page

1. REPORT STRUCTURE

This report deals with the development and application of a new diagnostic technique that has provided new information for the study of laser-plasma interactions. Spatially and temporally resolved observation of light emissions from a plasma at the second and three-halves harmonics of the incident laser light frequency has directly yielded plasma density profile information. These results are applied to the study of fundamental plasma processes: laser light absorption, energy transport, and hydrodynamics.

Chapter 2 provides an introduction to the topic of laser produced plasmas and to their study through the observation of harmonic light emissions. Chapter 3 deals with the procedures for data acquisition. Data accuracy requirements are put forth. The experimental setup for spatially and temporally resolved microscopy of laser produced plasmas is described. System resolution is determined and an image analysis procedure is put forth for the enhancement of the accuracy of the results. (Resolution determination procedures and formulation of the image analysis technique are detailed in Appendix A.) The final accuracy of the results is tabulated.

In Chapter 4 typical data is taken and reduced according to standard procedures. In Chapter 5 the experimental results are presented. Chapter 6 deals with the topics to which the experimental results are applied. Chapter 7 gives a discussion of the results.

Appendix B indicates the source of the harmonic emission spatial inhomogeneity.

Equations are in cgs units with electro-magnetic quantities in Gaussian units. Exceptions to this rule are found when a unit of length may be expressed in microns (1 μm = 10^{-4}cm), a unit of time may be expressed in picoseconds (1 psec = 10^{-12} sec.), a unit of power may be expressed in watts (1 watt = 10^{7} $\frac{\text{erg}}{\text{sec}}$), and a unit of temperature may be expressed in kilo-electron volts or electron volts (1 keV = 10^{3} eV = 1.16 x 10^{7} ^{o}k).

2. Introduction

The interaction of laser light with matter produces plasma that is inherently spatially inhomogeneous. Plasma generated at the surface of a solid target expands, and decreases in density. The density of target material increases due to shock wave compression. Induced target motion may cause density variation effects.

Typical computer predicted electron density and temperature profiles are shown in figure 2-1. The plasma has been generated from a thin spherical glass shell target irradiated with 1.06 μm wavelength laser light. The laser light (ω_o), propagating parallel to the density gradient, penetrates up to the critical electron density and is there reflected. Energy is absorbed by the plasma in the zone of light penetration. Energy deposited by the laser heats the plasma in the subcritical density region, the corona, to about 10^7 ^oK. Energy transported inwards through the critical surface generates hot plasma from the shell material. Momentum transferred from the outward ablating plasma drives the shell inwards. Dividing the inward and outward moving material is a point of zero velocity known as the ablation surface.

Of importance in the study of laser produced plasmas is the characterization of the electron density profile in the region of the critical density. Processes such as laser light absorption and plasma energy transport depend on and affect the critical density region profile. Profile modification may occur through the deposition into the plasma of laser light momentum.

The important possible light absorption mechanisms are collisional,

FIGURE 2-1

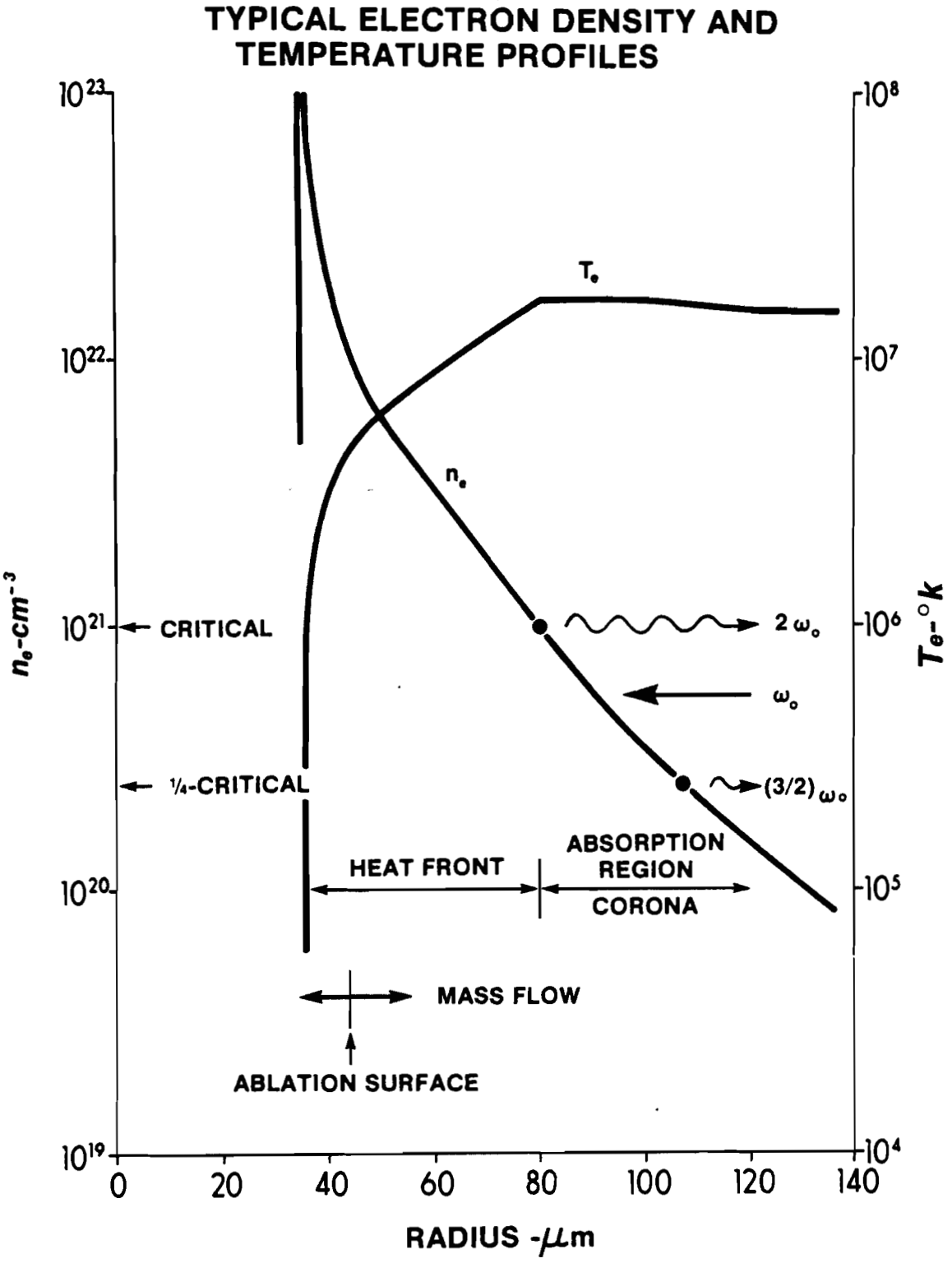
TYPICAL ELECTRON DENSITY AND TEMPERATURE PROFILES
10^{23}
10^{22}
10^{21}
10^{20}
10^{19}
10^{8}
10^{7}
10^{6}
10^{5}
10^{4}
n_e-cm^{-3}
T_e-°k
T_e
n_e
CRITICAL
¼-CRITICAL
2 ω_o
ω_o
(3/2) ω_o
HEAT FRONT
ABSORPTION REGION
CORONA
MASS FLOW
ABLATION SURFACE
0
20
40
60
80
100
120
140
RADIUS -μm

resonant, and plasma instability absorption. In collisional absorption, electrons driven by the laser light electric field collide with ions within the range of either a Debye shielding length (inverse bremsstrahlung absorption)[2-1,2,3] or a turbulent ion structure (absorption off of ion turbulence).[2-4,5,6,7] Collisional absorption is strongest where the frequency of collisions is largest. This occurs in the highest density region of light propagation, i.e., in the critical density region. Resonant absorption occurs when a component of the laser light electric field is converted directly into electron plasma waves.[2-8,9,10,11,12] The point where the plasma waves build up is at the critical density. Plasma instabilities absorb energy by coupling light into plasma oscillations.[2-13-22] These instabilities are resonant at various densities and, therefore, depend on the shape of the sub-critical density profile.

Collisional and resonant absorption have significant and relatively straightforward density scalelength dependences. Measurement of scalelength and absorption can, and does, allow theory and experiment to be compared. The density profile dependence of plasma instabilities is complicated by the requirement of knowing not only thresholds and growth-rates but also saturation and energy dissipation mechanisms. Although the existence of finite amplitude plasma waves is supported by some of this thesis' experimental observations,[2-22] the energy absorbed into them is not studied here.

The principal modes of energy transport through the plasma are thermal electron heat conduction[2-7,23,24] and supra-thermal electron transport.[2-25,26] The two mechanisms are distinguished from one

another by the relative magnitudes of the electron collision length and the plasma thickness. When the distance between electron collisions is small compared to the density scalelengths, the electrons quickly become thermal and the transport is "diffusive". Suprathermal electron collision lengths are long compared to density scalelengths and the energy transport is "free-streaming". The magnitude and nature of energy transport manifests itself in the density profile shape and can be studied via analysis of experimentally determined profiles.

Laser light momentum deposition effects may manifest themselves in the density profile shape. These effects are generally localized to regions of strong laser light absorption, reflection, or refraction and are predicted to occur as localized steepening of the density gradients,[2-6,20,21,27] as turbulence and rippling of the critical density surface[2-28], or as radial plasma filaments and laser beam self-focusing.[2-29] Profile modification effects may need to be considered when the ratio of the radiation pressure 'p_{rad}' to the electron pressure 'p_e' is of order .1 or greater.[2-27] For normal incidence light reflected from a surface

$$\frac{p_{rad}}{p_e} \simeq \frac{2I}{c} \frac{1}{n_e k T_e} \qquad (2\text{-}1)$$

where 'I' is the laser intensity, 'n_e' is the electron density, 'T_e' is the electron temperature, 'c' is the speed of light, and 'k' is Boltzmann's constant. For 1.06 μm light reflected from the critical

surface of a $1x10^{7}$ ^{o}k plasma, p_{rad}/p_e = .1 at a laser intensity of $I = 2x10^{21} \frac{erg}{sec\text{-}cm^2}$. Current experiments are conducted at laser intensities of $10^{22} \frac{erg}{sec\text{-}cm^2}$ or greater so that profile modification effects are predicted. At $10^{22} \frac{erg}{sec\text{-}cm^2}$ reference 2-27 predicts a density jump of $n_e=3x10^{20}$ cm^{-3} to $1.35x10^{21}$ cm^{-3} and reference 2-28 predicts the existence of critical surface turbulence.

Of particular interest for the experimental determination of the electron density profile in the critical density region is the generation in the plasma of light at harmonics of the laser light frequency. The emission of these harmonics is strongly density dependent so that within an inhomogeneous plasma the harmonic light emissions are localized to narrow intervals of density and space. By following the sources of harmonic light emissions, particular densities can be followed in space and time.

Spatially resolved observation of harmonic light emissions is the technique developed in this thesis. The harmonics viewed are the second ($2\omega_o$) and three halves ($\frac{3}{2}\omega_o$) harmonics of the incident laser light (ω_o). For laser light at a wavelength of 1.064 μm, the $2\omega_o$ occurs at .5320 μm (green) and the (3/2) ω_o occurs at .7093 μm (near infra-red). The $2\omega_o$ light is emitted at the critical density[2-30,31,32] $n_e = 1x10^{21}$ cm^{-3}, and the (3/2) ω_o is emitted at the quarter-critical density[2-17,33,34,35], $n_e = 2.5x10^{20}$ cm^{-3} (fig. 2-1). (See Appendix B)

As the plasma evolves, the critical and quarter-critical densities move in space and time. Spatially and temporally resolved $2\omega_o$ and (3/2) ω_o images provide critical and quarter-critical surface

trajectories (r_{cr}, $r_{\frac{1}{4}cr}$). Time resolved plasma density scalelengths are obtained as the difference between the quarter-critical and critical surface locations, i.e.,

$$\ell \equiv r_{\frac{1}{4}cr} - r_{cr} \tag{2-2}$$

Time integrated $2\omega_o$ and $(3/2)\omega_o$ images provide critical and quarter-critical surface peak excursions and a "characteristic" plasma density scalelength given by

$$L \equiv r_{\frac{1}{4}cr\ max} - r_{cr\ max} \tag{2-3}$$

In the experimental arrangement, figure 2-2, the four beam output of a Nd:glass laser is focused within a plane onto glass microballoon targets.[2-36] The $2\omega_o$ and $(3/2)\omega_o$ plasma emissions are viewed from a direction perpendicular to the plane of irradiation. The time resolved images obtained with a streak camera (section 3.1) record plasma emissions along an axis through two opposing beams. For any shot, critical and quarter-critical surface trajectories are obtained on opposing sides of the plasma. The time integrated photographs record the plasma emissions from each of the four laser beams so that peak excursion data is obtained within each of the focal spots.

FIGURE 2-2

EXPERIMENTAL ARRANGEMENT

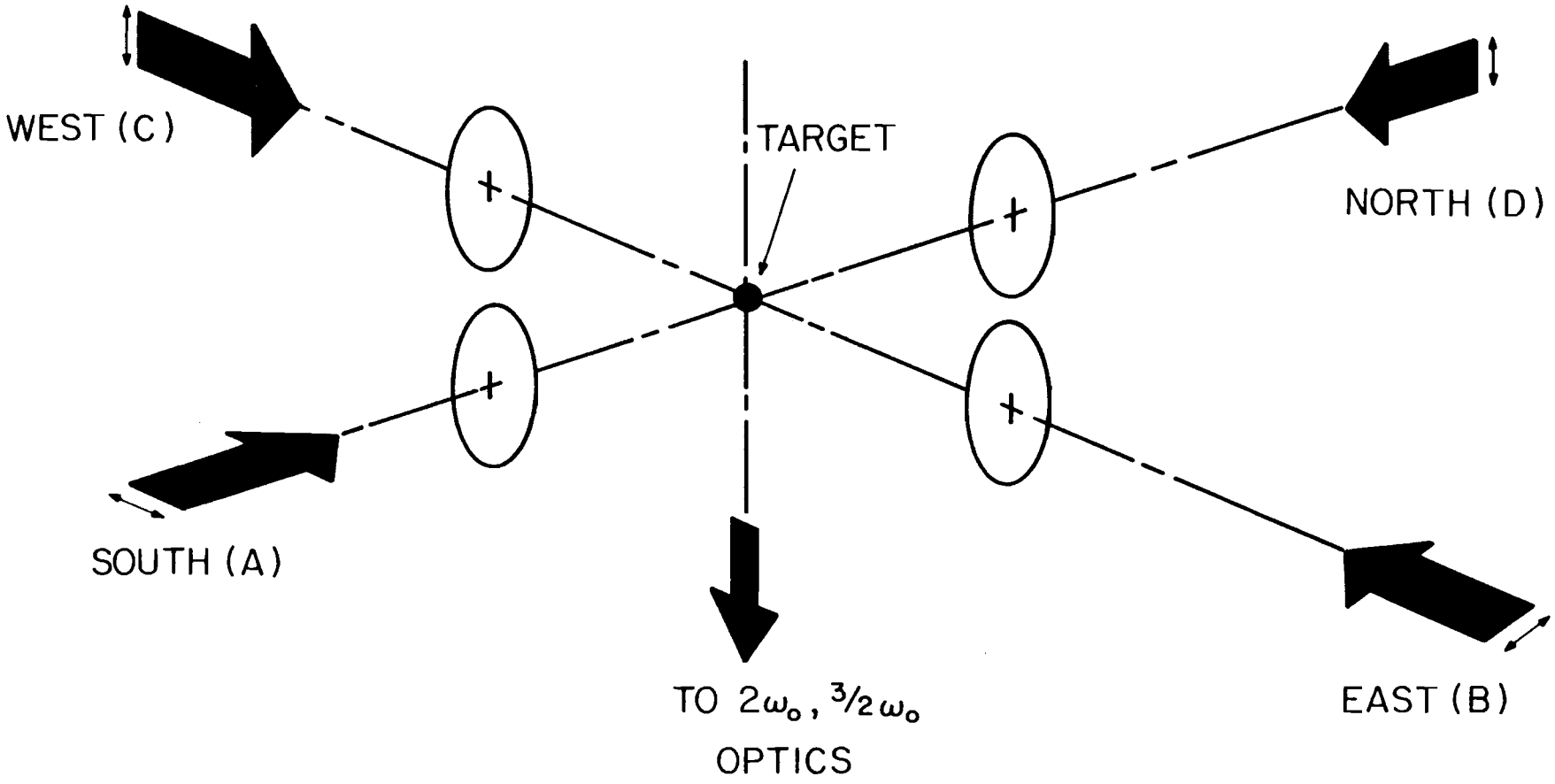

3. Data Acquisition and Accuracy

3.1 Experimental Setup

A schematic of the optical system is shown in figure 3-1. The system was designed to serve as an achromatic microscope for spatially and temporally resolved harmonic emission studies. Time integrated data with two dimensional spatial resolution was obtained by forming magnified images of the harmonic emissions on film. Temporal resolution was achieved by relaying the magnified images through a streak camera. The streak camera operated by displacing as a function of time the image of a slit located at the camera's entrance. Only the emission images falling on the entrance slit were relayed so that only one axis of the plasma was temporally and spatially resolved. Streaked data for the two harmonics was simultaneously obtained by placing the $2\omega_0$ and $(3/2)\ \omega_0$ images side-by-side on the streak camera entrance slit. The harmonic data was temporally multiplexed with the incident laser pulse via control of optical path lengths. The ω_0 light entered the streak camera earlier than the harmonic images so that the data was displaced in the output. (See figure 4-1.)

The hostile environment near the plasma necessitated the use of a long focal length lens to collect the light from the plasma. The necessity of imaging through a 1.3 cm thick vacuum chamber window required the placement of the first lens within the vacuum. To minimize spherical aberration caused by the window,[3-1] the first lens was placed one focal length from the target so that the light coming out was "collimated". The image produced by this lens was focused at

FIGURE 3-1

HARMONIC EMISSION VIEWING OPTICS

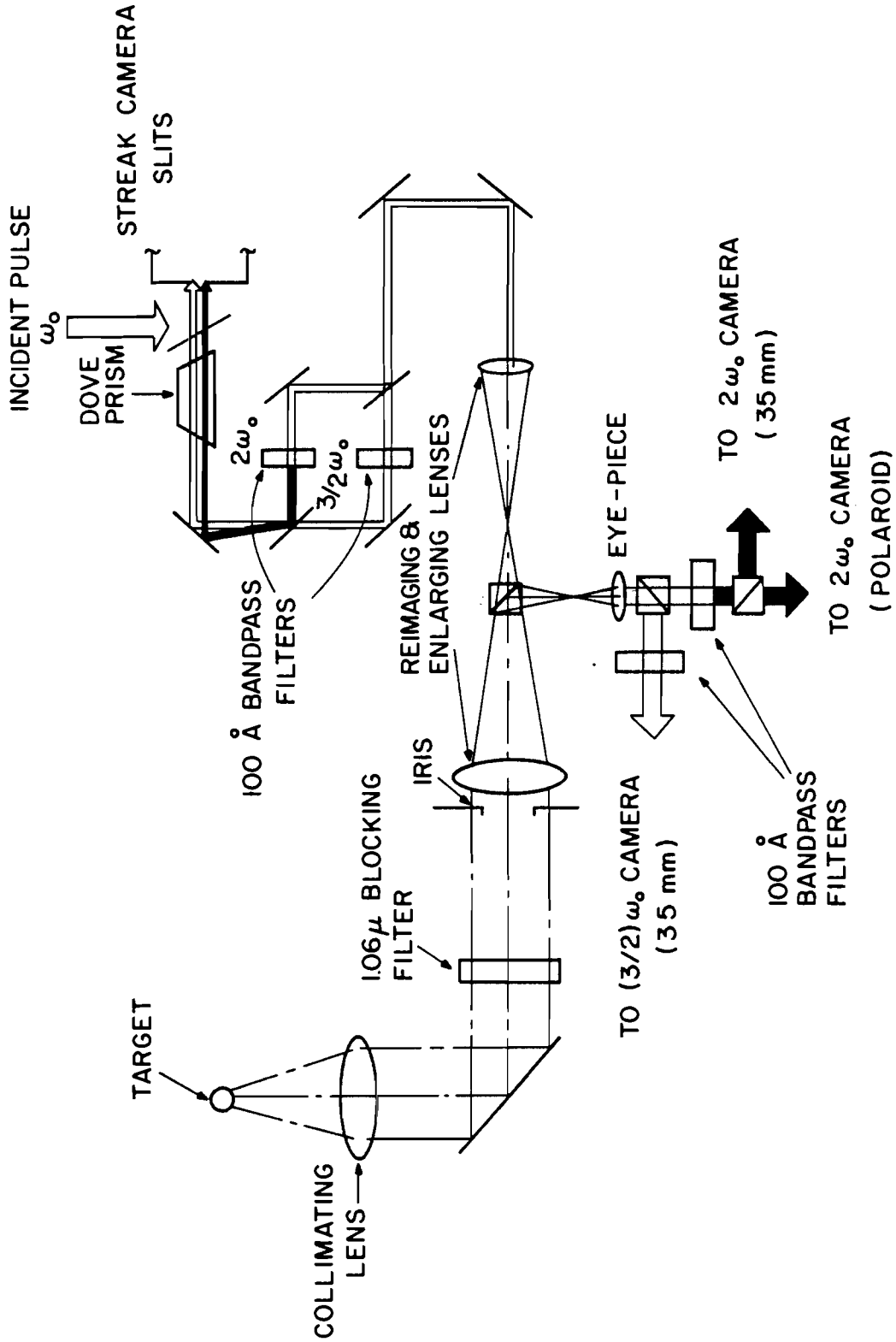

infinity. The collimating lens had a focal length of F_c = 20 cm and an f-number (f ≃ 1/full acceptance angle of lens) of f_c = 3.5.

The collimated light was readily relayed with λ/10 aluminum coated mirrors to a reimaging lens. An astronomical telescope objective, designed to image the collimated light from infinitely distant objects, was well suited for reimaging the plasma emissions. A Unitron telescope objective was used having a focal length of F_o = 150 cm and an f-number = 15.

The magnification of a two lens system of the type used can be calculated with reference to figure 3-2. Consider two rays leaving an object at height x_o. The first ray, 'a', is chosen so that it passes through the center of lens 1. In the approximation of a thin lens its path is undeviated and it passes in a straight line from the object point to the second lens. At the second lens the ray is refracted and it then passes on to the image plane. For the second ray, 'b', a ray is chosen such that after refraction by lens 1 it passes through the center of lens 2. Ray 'b' passes from lens 1 to the image point in a straight line. Since both rays leave the same point on an object one focal length from lens 1, both rays are parallel in the interval between the two lenses.

The angle 'α_1' that ray 'a' makes with the optical axis before hitting lens 2 is given by

$$\tan \alpha_1 = \frac{x_o}{F_1} \qquad (3\text{-}1a)$$

The angle 'α_2' that ray 'b' makes with the optical axis after pas-

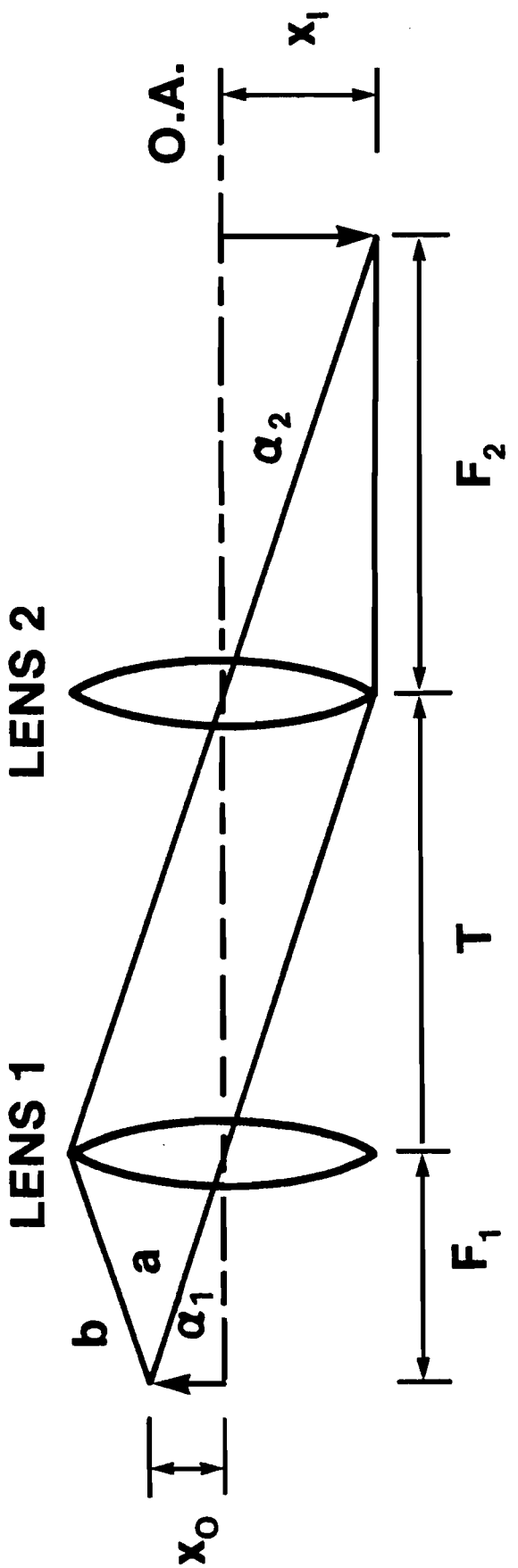

BASIC TWO LENS RELAY SYSTEM OF THE OPTICAL SYSTEM

FIGURE 3-2

sing through lens 1 is given by

$$\tan \alpha_2 = -\frac{x_I}{F_2} \tag{3-1b}$$

Since the two rays are parallel in the region between the lenses

$\alpha_1 = \alpha_2$

$$\frac{x_o}{F_1} = -\frac{x_I}{F_2}$$

The magnification 'm' is defined as the image height divided by the object height and for the two lens system is given by

$$m \equiv \frac{x_I}{x_o} = -\frac{F_2}{F_1} \tag{3-2}$$

At the telescope objective image plane the image was magnified by -7.5.

Additional magnification for the time integrated photographs was obtained with a second two lens system of the type just described. The two lenses were a telescope eye-piece with a focal length of F_e = 2.5 cm and a 35 mm camera lens with a focal length of F_1 = 5.5 cm. The total magnification of the system for the time integrated exposures was

$$m_{IO} = \frac{F_o}{F_c} \times \frac{F_1}{F_e} = 16.5 \text{ -- TIME INTEGRATED} \tag{3-3}$$

An advantage of the two lens arrangement was the magnification's independence to the distance between the lenses. The placement of the telescope objective and the camera lens was not critical. Another practical advantage was that the correct focus of the eye-piece in the two lens combination was also the proper focus for visual observations of the target through the eye-piece. The system could be visually aligned and focused, and a prefocused camera could then be put into place.

Space and alignment problems prohibited the use of a two lens system to relay a magnified image to the streak camera. A single F_s = 30 cm focal length Wray London Lustar process lens was used. The system magnification to the streak camera was

$$m_{so} = \left(\frac{-F_o}{F_c}\right)\left[\frac{-L - (L^2 - 4LF_s)^{\frac{1}{2}}}{-L + (L^2 - 4LF_s)^{\frac{1}{2}}}\right] = 19.5 \text{ -- ONTO STREAK CAMERA SLITS} \qquad (3\text{-}4)$$

where L = 160 cm was the distance from the telescope objective focus to the streak camera slits and F_s = 30 cm. Since the magnification in equation (3-4) was sensitive to changes in L it was checked by photographing a test object of known size through the viewing optics-streak camera system.

A rule of thumb in optics is that the introduction of elements into an optical system, generally, only degrades the final image quality. If elements must be introduced into a microscope system then they should be placed after as much magnification as possible has

been done so as not to magnify the aberrations introduced by the elements. With the exception of a 1.06 μm blocking filter this rule was followed for all beam splitters and filters. The effect of the 1.06 μm blocking filter was checked and found to be minimal.

The 1.06 μm blocking filter was a .2 cm thick Schott KG3 grade A filter. It had a transmission of 10^{-3} at 1.06 μm, .45 at .71 μm, and .88 at.53 μm. The interference filters were a Ditric .01 μm bandwidth .53 μm bandpass filter and a Bausch & Lomb .01 μm bandwidth .71 μm bandpass filter. Both filters had quoted rejection ratios of 10^4 and were measured to have rejection ratios of greater than the 10^2 sensitibity of the Cary 14 spectrometer on which they were tested.

The two remaining optical components were a variable aperture size iris and a dove prism. The iris was used to control aberrations through adjustment of the system f-number. (See section 3.3) The dove prism, a device used to rotate an image about the optical axis, was used to control the plasma axis being imaged through the streak camera.

Films used were chosen to have high sensitivity at the $2\omega_o$ and $(3/2)\ \omega_o$ frequencies. Kodak Tri-X Panchromatic and Kodak High Speed Infra-Red film[3-2] were chosen respectively for the $2\omega_o$ and $(3/2)\ \omega_o$ time integrated observations. Both films were developed in D-19 developer at 20^oC. The tri-X was developed for 4 minutes and the HSIR was developed for 9 minutes.

The streak camera was a model 512 Electro-Photonics electro-optic streak camera. A schematic is shown in figure 3-3. Its use

FIGURE 3-3

STREAK CAMERA SCHEMATIC

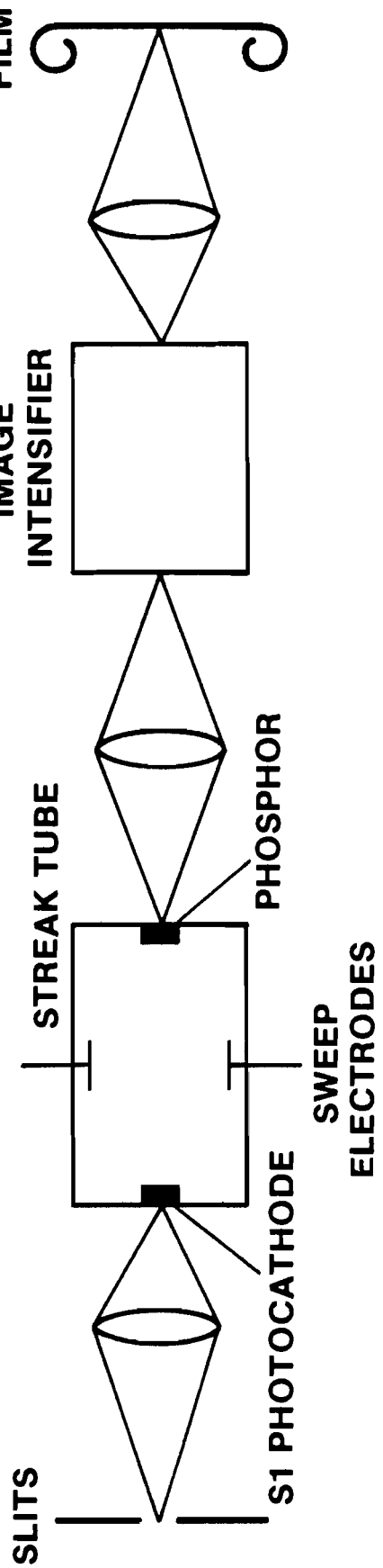

provided time resolved data with spatial resolution in one dimension. To briefly describe its operation; an entrance slit was optically imaged onto a photocathode within the streak tube. Electrons were emitted from the photocathode according to the intensity distribution of the light on its surface. The electrons were relayed through the streak tube and onto a phosphor output with electron optics. The output image was displaced in space (the input image in time) by applying a time varying electric field across the electron beam. At different times the slit image fell at different positions along the phosphor and a time resolved image of the input slit was obtained. The phosphor converted the electron image into a photon image. This image was optically coupled to a 4 stage magnetically focused image intensifier with a gain of 10^6. The output was placed onto photographic film to form a permanent record. Details on streak camera characteristics can be found in references (3-3) to (3-5).

3.2 Resolution Requirements

A primary consideration in the design of the experimental equipment was the required resolution. The resolution requirements were based on a consideration of the accuracy necessary to study the physics of light absorption and ablation region hydrodynamics, and of the accuracy of the other diagnostics to which the experimental results were compared. Resolution breaks down into two categories: spatial resolution and temporal resolution.

3.2.1 Spatial Resolution

There are two spatial length scales of interest. They are the

radius of the critical surface and the distance between the critical and quarter-critical surfaces.

To compare the experimental results to hydrodynamic codes and analytic models of plasma expansion it is sufficient to know the critical surface location to $\pm$ 5%. The critical surface position varies from the initial target radius ($\simeq$ 50 μm) to a maximum excursion of about 80 μm so that the accuracy requirement on the critical surface position is approximately $\pm$ 3 μm.

An important use of scalelength information is to examine the mechanisms for light absorption by a plasma. This is done by taking the measured scalelengths and calculating with the possible absorption mechanism theories, the energy fraction absorbed. This quantity is compared to the experimentally measured value of the fractional absorption (energy absorbed/energy on target). To accomplish this comparison, the accuracy of the scalelength measurement should be such that the calculated fractional absorption is at least as accurate as the measured fractional absorption.

Typical experimental values for the fractional absorption of 1.06 μm laser light, measured using a variety of techniques, is about .40 with measuremental accuracy of $\pm$ .08.[3-6,7,8,9] Figure 3-4 shows the theoretical scalelength dependence of inverse bremsstrahlung plus resonant absorption for the conditions of this experiment (see Chapter 6). To study the absorption's scalelength dependence with the accuracy of the absorption measurement, figure 3-4 shows that it is necessary to have a scalelength accuracy of approximately $\pm$ 4 μm.

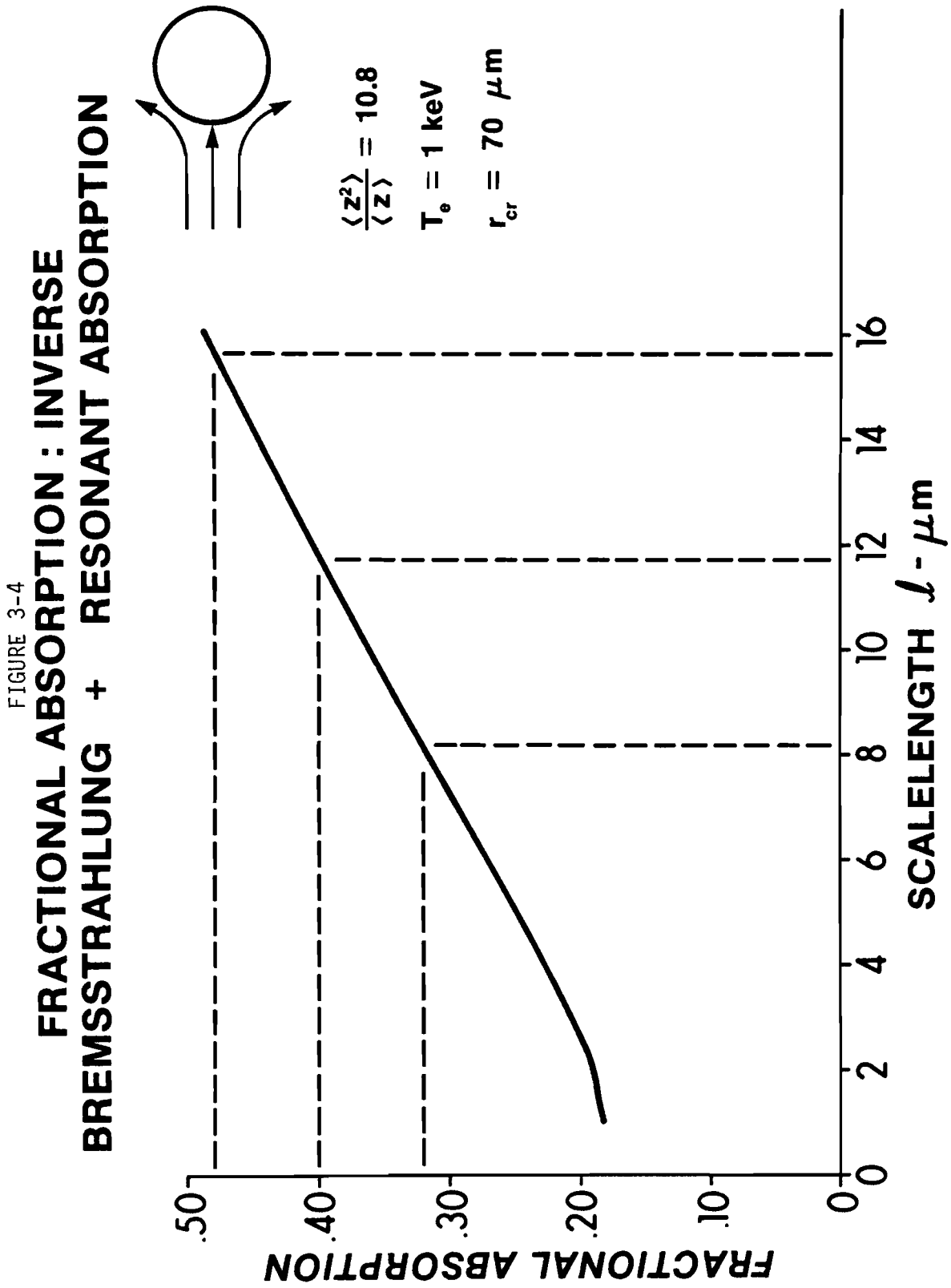
FRACTIONAL ABSORPTION : INVERSE
BREMSSTRAHLUNG + RESONANT ABSORPTION
$\frac{\langle z^2 \rangle}{\langle z \rangle} = 10.8$
$T_e = 1$ keV
$r_{cr} = 70\ \mu m$
FRACTIONAL ABSORPTION
.50
.40
.30
.20
.10
0
0
2
4
6
8
10
12
14
16
SCALELENGTH l - μm

FIGURE 3-4

3.2.2 Temporal Resolution

For the time-resolved results the desired temporal resolution is fixed by the spatial resolution and the maximum observed critical and quarter-critical surface expansion velocities.

The relationship between spatial and temporal resolution requirements can be seen by noting that if a position 'z' is measured at time 't' then the next measurement should be made by the time the position has changed by one resolution element 'ℓ'. At a velocity 'v', the position will have changed by 'ℓ' in a time 'δt' given by:

$$\delta t = \frac{\ell}{v} \tag{3-5}$$

The most stringent requirement on temporal resolution occurs when v is a maximum. The maximum velocity observed is on the order of 5×10^7 cm/sec. This leads to a temporal resolution requirement of $\delta t = \pm 6$ psec.

3.3 Sources of Spatial Error

Principal sources of error in making spatial measurements are the finite thickness of the object, the finite diffraction limited resolution of the optical system, the aberrations present in the optics and streak camera, and distortion produced by refraction of light as it passes out of the plasma. Error due to the first three sources results from the necessity of analyzing photographs that contain blurred images. The effect of the last source of error,

refraction, is the production of an emitting surface image that is possibly distorted from the actual emitting surface shape lying within the plasma.

Finite object thickness and diffraction limited resolution produce an upper limit on the theoretical resolution of the optical system. Real lens and streak camera aberrations degrade the actual resolution from the theoretical value.

In this section the effect of each source of error on the system resolution is characterized. Theoretical and actual resolutions are compared. Bounds are placed on the possible error due to light refraction by the plasma. The section concludes with a description of a simple image analysis technique that accounts for and eliminates most of the systematic error introduced by the finite system resolution.

Only results as they pertain to the accuracy of the $2\omega_0$-$(3/2)\ \omega_0$ measurements are described in this section. Detailed derivations and general aspects of spatial resolution measurements are described in the appendix. Included in the appendix are new results on the intensity dependence of the streak camera spatial resolution.

3.3.1 Theoretical Spatial Resolution

Limitations on the ultimate resolution of any optical system are imposed by the finite thickness of the object being viewed and by the diffraction limited performance of the optics used to collect and reimage the light.

Finite object thickness effects arise from the fact that a well corrected optical system images a plane object into a plane image.

The image of a three-dimensional object can have only a single plane in sharp focus. The rest of the object appears blurred to some extent. Even if only a single plane is being studied, the effect of the entire object must be considered since, in general, light from out-of-focus points overlaps the in-focus points.

The amount of blurring due to the finite object thickness is a function of the object thickness parallel to the optical axis, the object shape, and the angular spread in the rays leaving the object and collected by the optics. The effect can be expressed in terms of a point or edge resolution. Point resolution gives the blur in individual out-of-focus points and can be quantified as the blur circle radius. Edge resolution gives the blur observed at the outer edge of a three-dimensional object and can be expressed as the difference between the actual edge location and the location in the image of the outermost blurred light.

Diffraction limited performance is a consequence of the limited collection angle of the optics. To form a perfect image of a point, all of the emitted light must be collected and reimaged. The inability to do so results in an emitting point image consisting of an "Airy diffraction pattern".(3-10) The image spot size, quantified as the diffraction pattern radius at the first intensity minimum, is a function of the angular spread in the light collected and of the light wavelength.

The resolution of a diffraction limited system viewing a spherical object is given by equation (3-6) for the point resolution 'r_p'

and equation (3-7) for the edge resolution '$\mathcal{R}_E$'.

$$\mathcal{R}_p = \left[\left(\frac{x}{2f_c}\right)^2 + (1.22\lambda f_c)^2\right]^{\frac{1}{2}} \tag{3-6}$$

$$\mathcal{R}_E = \left[\left(\frac{r}{8f_c^2}\right)^2 + (1.22\lambda f_c)^2\right]^{\frac{1}{2}} \tag{3-7}$$

'λ' is the light wavelength, 'f_c' is the dimensionless f-number of the collecting optics, 'x' is the distance parallel to the optical axis from the object point to the plane of best focus, and 'r' is the radius of the emitting surface. The first term in equations (3-6) and (3-7) gives the contribution due to the finite object thickness and the second term gives the contribution due to diffraction limited performance.

Figures 3-5 and 3-6 show plots of equations (3-6) and (3-7) for conditions of experimental interest. At low f-numbers (large collection angles) finite object thickness effects dominate while at high f-numbers diffraction limitation effects dominate. Optimum resolution can be achieved via adjustment of f_c although the optimum point and edge resolutions do not coincide. The point resolution is relatively insensitive to the source location (x) for $f_c \gtrsim 12$ while edge resolution is independent of the emitting object radius (r) for $f_c \gtrsim 5$. (The independence of $\mathcal{R}$ on object parameters shall prove to be of importance when image analysis is considered.)

3.3.2 Actual Spatial Resolution

The actual optical system was run at an f-number of f_c=13. This

FIGURE 3-5

RESOLUTION OF A POINT AT A HEIGHT x ABOVE THE PLANE OF BEST FOCUS

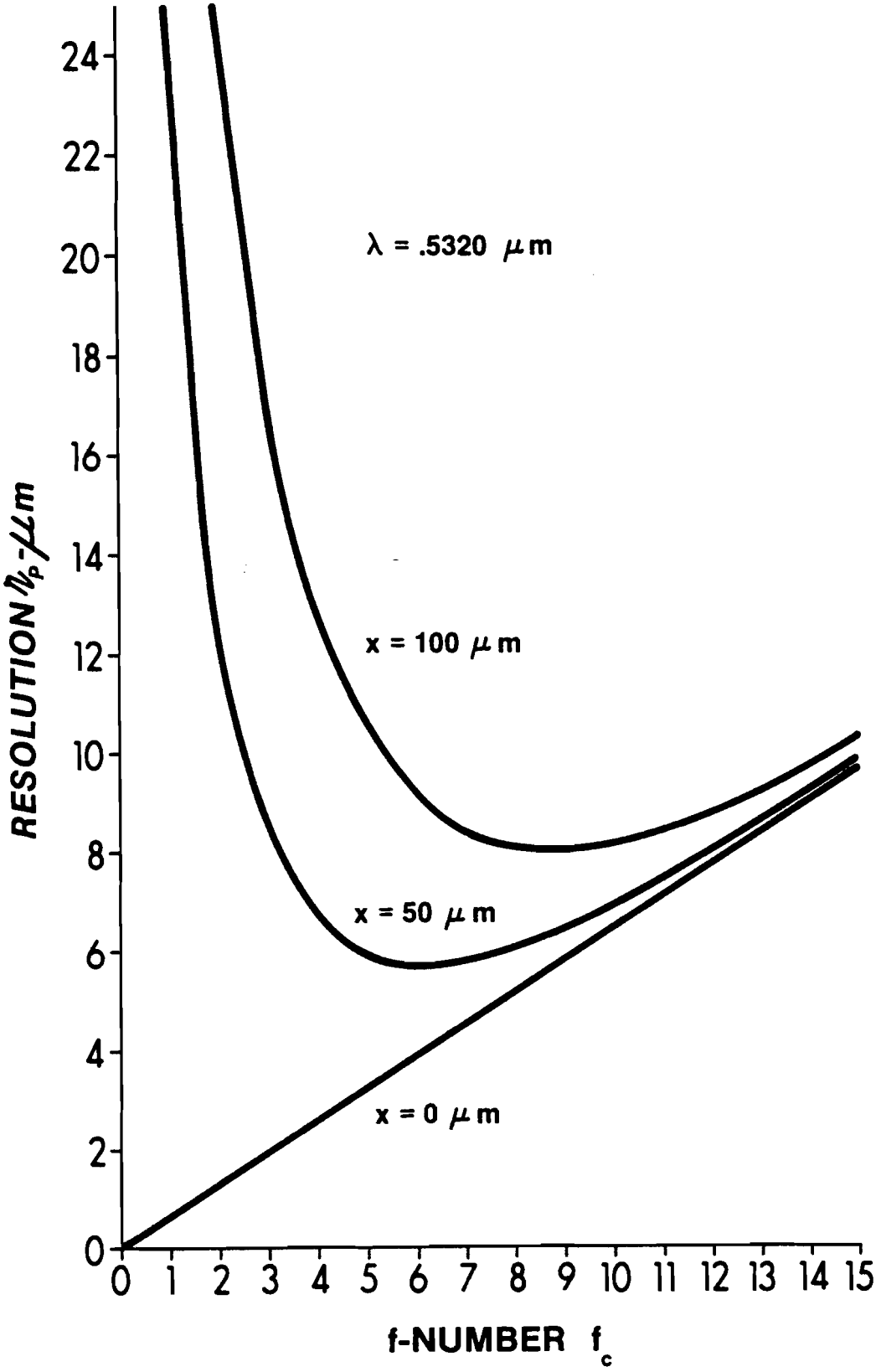

FIGURE 3-6

RESOLUTION OF AN EDGE FOR EMITTING SURFACES WITH RADIUS r.

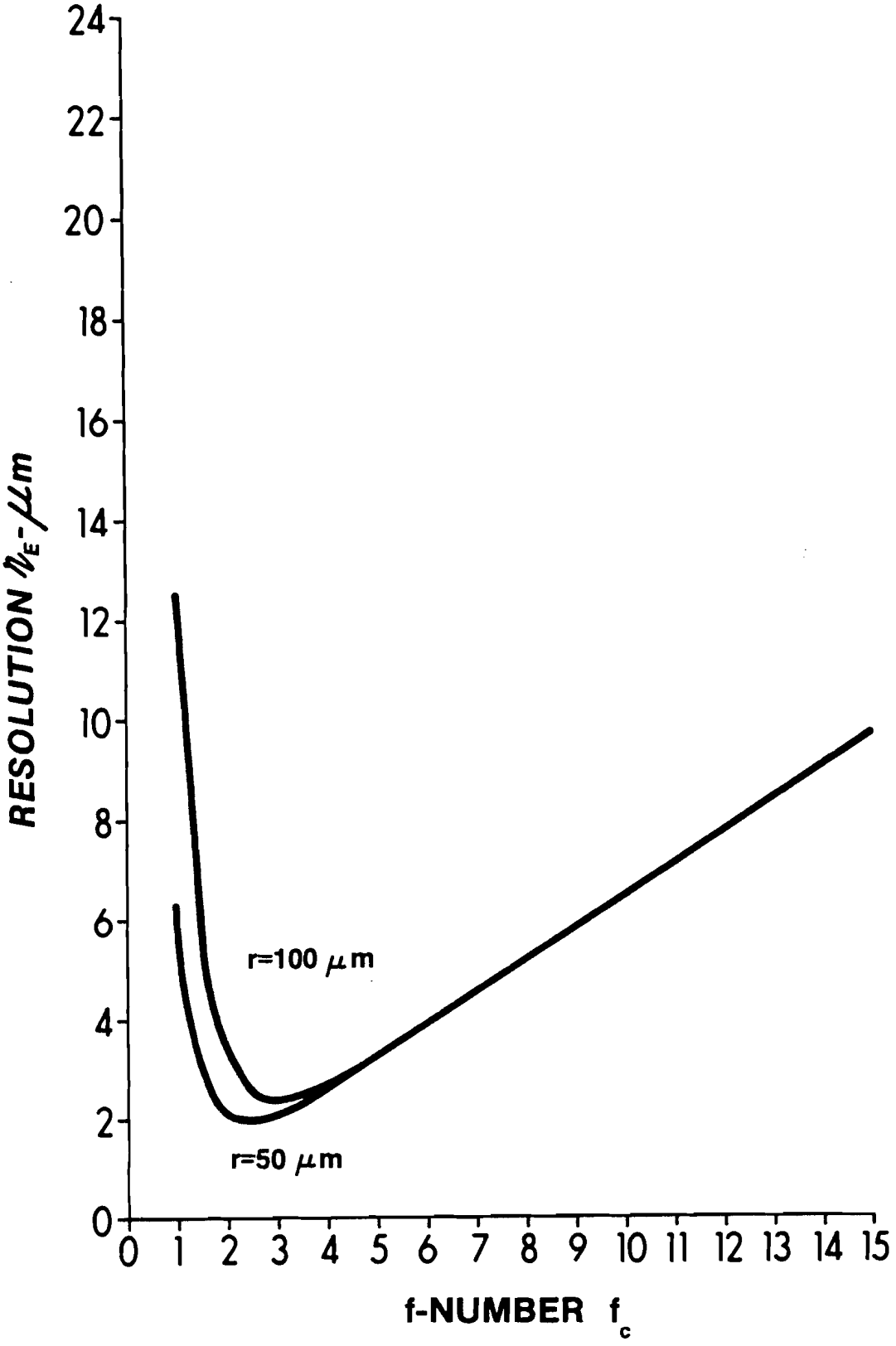

was the lowest collimating lens f-number for which the non-symmetrical aberration of coma was eliminated,[3-11] and for which the symmetrical aberrations of spherical and axial chromatic aberration[3-11] were reduced to the point where a point source Airy diffraction pattern could be clearly observed.[3-12] The resolution, exclusive of the streak camera, was determined by photographing resolution charts and test objects and was found to be 8 to 9 μm with green light (λ = .53 μm) illumination. This is in good agreement with the 8 μm prediction of near diffraction limited performance. White light illumination revealed no significant axial or lateral chromatic aberration.

Using equation (3-6), the flat object resolution for the two wavelengths of interest are: 8 μm at λ = .5320 μm and 11 μm at λ = .7093 μm.

Relaying the images through the streak camera degraded the resolution from that of the passive optical system. Resolution measurements were made in static and streaked modes and the principal results are: the intensity distribution of the point response shows only a weak broadening with increasing input intensity, the width of the point response at the noise level increases but that this broadening is due to a minimum detection level so that more of the point response is seen for more intense inputs, and the streak camera spatial resolution degrades by 25% in going from static to streaked mode.

The width of the point response at the noise level is the important measure of resolution for the experimental results. A plot of the streaked data resolution as measured by the point response half width at base density, as a function of the peak film exposure is shown in figure 3-7. The resolution is referenced back to the plasma.